PTEP

Prog. Theor. Exp. Phys. **2014**, 013B02 (21 pages)
DOI: 10.1093/ptep/ptt118

Iodine molecule for neutrino mass spectroscopy: ab initio calculation of spectral rate

Motomichi Tashiro[1,*], Masahiro Ehara[1], Susumu Kuma[2], Yuki Miyamoto[3], Noboru Sasao[2], Satoshi Uetake[4], and Motohiko Yoshimura[4,*]

[1]*Institute for Molecular Science, Nishigo-Naka 38, Myodaiji, Okazaki 444-8585, Japan*
[2]*Research Core for Extreme Quantum World, Okayama University, Okayama 700-8530, Japan*
[3]*Graduate School of Natural Science and Technology, Okayama University, Okayama 700-8530, Japan*
[4]*Center of Quantum Universe, Okayama University, Okayama 700-8530, Japan*
*E-mail: tashiro.motomichi@gmail.com, yoshim@fphy.hep.okayama-u.ac.jp

Received October 28, 2013; Accepted December 13, 2013; Published January 24, 2014

It has recently been argued that atoms and molecules may become good targets for determining neutrino parameters still undetermined, if the atomic/molecular process is enhanced by a new kind of coherence. We compute the photon energy spectrum rate arising from coherent radiative neutrino pair emission processes of metastable excited states of I_2 and its isovalent molecules, $|Av\rangle \to |Xv'\rangle + \gamma + \nu_i\nu_j$ and $|A'v\rangle \to |Xv'\rangle + \gamma + \nu_i\nu_j$, with γ an IR photon and $\nu_{i(j)}$ the $i(j)$th neutrino mass eigenstates, and show how fundamental neutrino parameters may be determined. Energies of electronically excited states of I_2, including the effect of spin–orbit couplings, were calculated by the multiconfigurational second-order perturbation (CASPT2) method. Summation over many vibrational levels of intermediate states is fully incorporated. Unlike atomic candidates with a much larger energy difference, such as Xe, I_2 transitions from a vibrational level $A(v = 0)$ to $X(v' = 24)$ give us an opportunity to determine the mass type (Majorana vs Dirac distinction) and the Majorana CPV (charge-conjugation parity violating) phases, although the rate is much smaller.

Subject Index B52, B54

1. Introduction

Neutrinos are the most common particles, next to 3 K photons, in the present universe, yet their properties have eluded comprehensive experimental determination since these neutral particles have only weak interaction. The conventional target for exploration of neutrino properties has been nuclei; stable nuclei in neutrino oscillation experiments and unstable nuclei in other neutrino experiments. The measured quantities derived so far by neutrino oscillation experiments are mass-squared differences ($\Delta m^2_{ij} \equiv m^2_i - m^2_j$) and mixing angles summarized [1][1] by

$$\Delta m^2_{21} \sim 7.5 \times 10^{-5}\,\mathrm{eV}^2, \quad |\Delta m^2_{31}| \sim 2.5 \times 10^{-3}\,\mathrm{eV}^2, \tag{1}$$

$$\sin^2\theta_{12} \sim 0.31, \quad \sin^2\theta_{23} \sim 0.42, \quad \sin^2\theta_{13} \sim 0.024. \tag{2}$$

[1] Other fits from Refs. [2,3] give almost identical values of mass-squared differences and θ_{12}, θ_{13}, but different numbers for θ_{23}, which is not used for our RENP rate calculation.

It has been assumed in this analysis that there exist only three kinds of neutrino, which we also follow throughout this work. The other hint to the absolute mass scale is derived from cosmological arguments, giving $\sum_i m_i < O(0.5)$ eV. (Cosmological bounds are summarized in Ref. [4]. They quote the bound $\Sigma_i m_i < (0.3\text{–}1.3)$ eV at 95% confidence level.) The important quantities undetermined in oscillation experiments are (1) absolute neutrino masses (impossible to determine in oscillation experiments), (2) CP symmetry (C = charge conjugation, P = parity) violating phase (CPV phase for short), and (3) whether the massive neutrino belongs to the Majorana type[2] or not.

There are two different kinds of ongoing experiments using unstable nuclei for measurements of still-undetermined neutrino parameters; (1) the end-point spectrum of beta decay of nuclei such as tritium for the measurement of an averaged absolute neutrino mass value, and (2) the search of neutrinoless double beta decay for verification of lepton number violation related to a finite Majorana type of masses. So far negative limits have been set in these experiments. The reason for the use of unstable nuclei is that the weak decay rate such as the nuclear beta decay increases with a high positive power of the released energy, usually the fifth power, and the available nuclear energy of a few MeV gives a detectable rate. But with the expected small neutrino mass of a fraction of eV, the energy mismatch becomes a serious problem, and the determination of the absolute neutrino mass value and exploration of undetermined important neutrino properties are more and more difficult.

With the advent of remarkable technological innovations, manipulation of atoms and molecules may contribute greatly to fundamental physics. Neutrino physics may also be one of these areas. Atoms and molecules are target candidates of precision neutrino mass spectroscopy, as recently emphasized in Ref. [5], due to the closeness of the energy released in their transition to expected neutrino masses. The process relevant to our interest is cooperative (and coherent, subsequently called macro-coherent) atomic de-excitation; $|e\rangle \to |g\rangle + \gamma + \nu_i \nu_j$, where $\nu_{i(j)}, i(j) = 1, 2, 3$ is one of the neutrino mass eigenstates. γ in the present work refers to a photon in the visible to the infrared region. The initial state $|e\rangle$ must be metastable, with a lifetime of, say, $\gtrsim O(1)$ msec. The process, as shown in Fig. 1, exists as a combined effect of second order in quantum electrodynamics (QED) and weak interaction of the standard electroweak theory[3].

To obtain a measurable rate for the process, it is crucial to develop macro-coherence [5,7], a new kind of coherence. The macro-coherent emission of radiative neutrino pairs is stimulated by two trigger irradiations of frequencies ω, ω' constrained by $\omega + \omega' = \epsilon_{eg}/\hbar$, $\omega < \omega'$, with $\epsilon_{eg} = \epsilon_e - \epsilon_g$ the energy difference of the initial and final states. The measured photon energy in the de-excitation is given by the smaller frequency ω. Macro-coherence ensures that the three-body process, $|e\rangle \to |g\rangle + \gamma + \nu_i \nu_j$, conserves both energy and momentum. Assuming that atoms in the states $|e\rangle$ and $|g\rangle$ can be taken infinitely heavy and that atomic recoil may be ignored, there exist threshold photon energies [8] at

$$\hbar\omega_{ij} = \frac{\epsilon_{eg}}{2} - \frac{(m_i c^2 + m_j c^2)^2}{2\epsilon_{eg}}. \tag{3}$$

[2] The massive Majorana neutrino is described by a relativistically covariant two-component spinor and satisfies the Majorana equation (unlike the Dirac equation for four-component spinors). The particle number is ill defined in the Majorana equation, and violates the U(1) symmetry associated with the lepton number. The quasi-particle of Majorana nature discussed in condensed matter physics is different in its dispersion relation from the massive Majorana neutrino in particle physics.

[3] The weak interaction Hamiltonian is adequately described here by the four-Fermi contact interaction. For relation to the W- and Z-exchange fundamental interaction in the standard electroweak theory, see any standard textbook, such as Ref. [6].

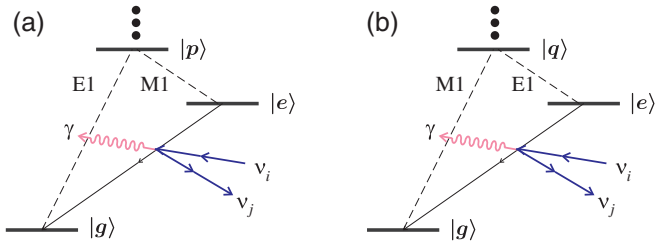

Fig. 1. Feynman-like diagrams for RENP from Λ-type atom/molecule, $|e\rangle \to |g\rangle + \gamma + \nu_i \nu_j$, with γ a photon and $\nu_{i(j)}$ a neutrino mass eigenstate. Virtual intermediate states $|p\rangle$, $|q\rangle$ should be summed over. The two-photon transition $|e\rangle \to |g\rangle + \gamma + \gamma$ may also occur via weak M1 × E1 or E1 × M1 couplings to $|p\rangle$ or $|q\rangle$.

Each time the emitted photon energy decreases below a fixed threshold energy of $\hbar\omega_{ij}$, a new continuous spectrum is opened; hence, there are six energy thresholds $\hbar\omega_{ij}$, $i, j = 1, 2, 3$ ((i, j) threshold for brevity) separated by finite photon energies. Determination of the threshold location given by Eq. (3), and hence decomposition into six mass thresholds, is made possible by the precision of irradiated laser frequencies at $\omega \approx \omega_{ij}$ and not by the resolution of the detected photon energy.

The macro-coherently amplified radiative emission of a neutrino pair has been called RENP (radiative emission of neutrino pair) [5], which is the core idea of our neutrino mass spectroscopy that may determine all unknown neutrino parameters. It has been argued that this method using atoms and molecules is ultimately capable of determining the nature of neutrino masses, the Dirac vs Majorana distinction, and measuring the new Majorana source of CPV phases [8,9]. It is crucial for explanation of the matter–antimatter asymmetry of the universe to verify the Majorana nature of neutrinos and determine CPV phases related to the Majorana case [10,11].

There is an important constraint on possible target atoms/molecules to obtain reasonable rates for realistic experiments. The atomic operator involved in RENP has the character of M1 × E1, where the M1 operator (actually electron spin $\vec{S}$ in subsequent RENP formulas) governs the weak interaction Hamiltonian of neutrino pair emission and the E1 operator denotes the usual dipole interaction of QED. The total angular momentum change via a virtual intermediate state requires that the LS coupling scheme should be broken [5]; hence, candidates should be sought in heavy atoms/molecules. In this way we identified the Xe atom as a good candidate.

The Xe atom is excellent, having a great discovery potential for the RENP process, and is further expected to determine the absolute neutrino mass scale and distinguish the normal mass vs the inverted mass hierarchy (denoted by NH and IH, respectively) [5]. On the other hand, distinction of the mass type (Dirac vs Majorana) requires a smaller released energy, of order a fraction of 1 eV, as shown in Ref. [9]. In the present work we shall study I_2 and its isovalent molecules for this purpose.

Molecules have a number of merits for RENP: (1) homonuclear diatomic molecules such as I_2 have vibrational states among which the usual E1 transition (its Hamiltonian $\propto \vec{d} \cdot \vec{E}$) is forbidden, (2) the richness of the vibrational and rotational levels makes it ideal to perform a systematic search of neutrino mass thresholds. Moreover, the I_2 molecule has a number of metastable states with energies $\lesssim$1 eV above the vibrationally excited levels in the electronically ground state.

Electronic excited states of the I_2 molecule have been intensively investigated by quantum chemical calculations [12–14]. The potential energy curves (PECs) and spectroscopic constants as well as transition properties of this system have been well examined, while the spin operator element, which is relevant for the present neutrino mass spectroscopy, has not been focused on so much. In this work

we shall present the RENP spectral rate using molecular wavefunctions based on a first-principles calculation.

We show in the present work that the proposed I_2 de-excitation scheme gives an opportunity to take measurements, clarify the Majorana vs Dirac distinction, and determine the CPV phases, which are, in the quasi-degenerate case of neutrino masses, easier than the NH vs IH distinction at low photon energies where rates are largest. A good sensitivity of the spectral shape to determination of the smallest neutrino mass of order meV is also shown for this target molecule.

Throughout this work we assume the macro-coherent mechanism as proposed in Ref. [5]. We also use natural units of $\hbar = 1, c = 1$, except in Sect. 3, where atomic units are used following the standard practice of quantum chemistry.

2. RENP amplitude and rate formula

We shall recapitulate from Ref. [5] the main features of the spectral formulas.

The amplitude corresponding to the Feynman-like diagram of Fig. 1 is given by the electroweak theory and reads

$$\mathcal{M} = G_F \vec{E} \cdot \left(\sum_p \frac{\langle g|\vec{d}|p\rangle\langle p|\vec{S}|e\rangle}{\epsilon_{pg} - \omega} + \sum_q \frac{\langle q|\vec{d}|e\rangle\langle g|\vec{S}|q\rangle}{\epsilon_{qg} - \omega} \right) \cdot \sum_{ij} a_{ij} \nu_j^\dagger \vec{\sigma} \nu_i, \tag{4}$$

$$a_{ij} = U_{ei}^* U_{ej} - \frac{1}{2}\delta_{ij}, \tag{5}$$

where U_{ei} (their relation to necessary mixing angles and CPV phases given in Eq. (18)) is the matrix element of neutrino mixing (expressions in terms of measurable quantities given later), and $\nu_i(\vec{p}, h)$ the neutrino plane wavefunction of momentum $\vec{p}$ and helicity h of mass m_i, $\vec{E}$ the electric field of the irradiated trigger laser of frequency $\omega < \epsilon_{eg}/2$, $\vec{S}$ the electron spin operator, and $\vec{d}$ the electric dipole operator. Quantum numbers of states should include all the electronic, vibrational, and rotational ones. The sum over all vibrational modes of the intermediate states, $|p\rangle$ and $|q\rangle$, is particularly important for molecules. For simplicity we ignore the Hönl–London factor (see, e.g., Ref. [15]) of order unity, assuming that rotational degrees of freedom are frozen.

The two terms in brackets on the right-hand side of Eq. (4) correspond to two different vertices, the weak M1 type of neutrino pair emission (its Hamiltonian $\sim G_F \vec{S} \cdot \nu_j^\dagger \vec{\sigma} \nu_i$) and the QED E1 transition vertex in the second-order perturbation theory as depicted in Fig. 1: the first term of the molecular state change of $|e\rangle \to |p\rangle \to |g\rangle$ shall be designated by E1 × M1 and called (a) in the figure, and the second term of the molecular state change of $|e\rangle \to |q\rangle \to |g\rangle$ shall be designated by M1 × E1 and called (b). Both states $|p\rangle$, $|q\rangle$ are summed over, since they are virtual intermediate states.

For an isotropic medium without directional alignment by a magnetic field, this amplitude squared gives the basic rate formula (omitting the second contribution $C^b(\omega)$ from $|q\rangle$ in Eq. (4)):

$$\Gamma_{\gamma 2\nu}(\omega) = \Gamma_{dm} C^a(\omega) I(\omega), \tag{6}$$

$$\Gamma_{dm} = \frac{G_F^2 |\vec{E}|^2 n^2 V}{18\pi\bar{\epsilon}^2}, \tag{7}$$

$$C^a(\omega) = \bar{\epsilon}^4 \sum_p \frac{\langle g|\vec{d}|p\rangle \cdot \langle p|\vec{d}|g\rangle \langle e|\vec{S}|p\rangle \cdot \langle p|\vec{S}|e\rangle}{(\epsilon_{pg} - \omega)^2}, \tag{8}$$

$$I(\omega) = \frac{1}{\bar{\epsilon}^2}\sum_{ij}(B_{ij}I_{ij}(\omega) + \delta_M B^M_{ij} I^M_{ij}(\omega))\theta(\omega_{ij} - \omega), \tag{9}$$

$$B_{ij} = |a_{ij}|^2, \quad B^M_{ij} = \Re(a^2_{ij}), \tag{10}$$

$$I_{ij}(\omega) = \Delta_{ij}(\omega)\left(\frac{1}{3}\epsilon_{eg}(\epsilon_{eg} - 2\omega) + \frac{1}{6}\omega^2 - \frac{1}{18}\omega^2\Delta^2_{ij}(\omega) - \frac{1}{6}(m_i^2 + m_j^2)\right.$$
$$\left. - \frac{1}{6}\frac{(\epsilon_{eg} - \omega)^2}{\epsilon^2_{eg}(\epsilon_{eg} - 2\omega)^2}(m_i^2 - m_j^2)^2\right), \tag{11}$$

$$I^M_{ij}(\omega) = -m_i m_j \Delta_{ij}(\omega), \tag{12}$$

$$\Delta_{ij}(\omega) = \frac{1}{\epsilon_{eg}(\epsilon_{eg} - 2\omega)}\left\{\left(\epsilon_{eg}(\epsilon_{eg} - 2\omega) - (m_i + m_j)^2\right)\left(\epsilon_{eg}(\epsilon_{eg} - 2\omega) - (m_i - m_j)^2\right)\right\}^{1/2}. \tag{13}$$

In the overall rate factor, Γ_{dm} for diatomic molecules, the directionality of trigger correlated with the molecular axis is taken into account by an extra 1/3 reduction factor. $\bar{\epsilon}$ is a reference energy, to make both $C^a(\omega)$ and $I(\omega)$ dimensionless. In the rest of this work we take $\bar{\epsilon} = \epsilon_{eg}$. The function $\theta(x) = 0$ for $x < 0, = 1$ for $x > 0$ is the step function, giving rise to six mass thresholds in Eq. (9).

$\delta_M = 1$ for the case of Majorana neutrinos and $\delta_M = 0$ for the Dirac neutrino. The term $\propto \delta_M$ exhibits the quantum mechanical interference intrinsic to identical fermions of Majorana particles [8], which arises from the antisymmetric wavefunctions of two identical fermions. For the Dirac neutrino case, the emitted particles (except the photon) are a neutrino and an anti-neutrino, two distinguishable particles, and hence the interference terms are absent.

For the stored field strength $|\vec{E}|^2$, we shall take its maximal value $\epsilon_{eg}n$, with n the number density of excited state targets. More generally, this rate should be multiplied by the dynamical factor $\eta_\omega(t)$, whose calculation requires the solution of the master equation given in Ref. [5]. It is important to keep in mind that the medium polarization $R_i, i = 1, 2$ between $|g\rangle$ and $|p\rangle$ states under trigger irradiation is contained in the dynamical factor given by

$$\eta_\omega(t) = \frac{1}{L}\int_0^L dx \frac{|\vec{E}(x)|^2|\langle p|(R_1 - iR_2)|g\rangle(x)|^2}{4\epsilon_{eg}n^3}, \tag{14}$$

an integrated quantity over the entire target at $0 \le x \le L$ along the trigger irradiation. Thus, a large macroscopic polarization is required for a large RENP rate. The overall maximal rate in units of 1/time is

$$\Gamma_{dm} = \frac{G_F^2 n^3 V}{18\pi\epsilon_{eg}} \sim 26\,\mathrm{kHz}\left(\frac{n}{10^{21}\,\mathrm{cm}^{-3}}\right)^3 \frac{V}{10^2\,\mathrm{cm}^3}\frac{0.810\,\mathrm{eV}}{\epsilon_{eg}}. \tag{15}$$

The spectral information is given by $I(\omega)$, which is calculated using neutrino parameters experimentally determined in Eq. (2). Calculation of the molecular factor $C(\omega)$ is the main subject of the next section.

3. Molecular factor

In this section, we investigate the possibility of the RENP experiment using the I_2 molecule, with the electronically ground state $X\,0^+_g$ as the $|g\rangle$ state and the (metastable) electronically excited states $A\,1_u$ and $A'\,2_u$ as the $|e\rangle$ state. One advantage of the $A'\,2_u$ state over the $A\,1_u$ state is its longer natural lifetime. In the simplified model for the RENP process $|A'v\rangle \to |Xv'\rangle + \gamma + \nu_i\nu_j$ in Ref. [5], only the I_2 $A\,1_u$ state is considered as the intermediate $|p\rangle$ state. However, other electronic states

may have a similar or larger contribution to the molecular factor. We first calculate the molecular factor including several I_2 excited electronic states in the intermediate state summation, without considering vibrational states. There, we examine (1) which intermediate electronic state contributes the most significantly to the molecular factor, and (2) the relative weight of the E1 × M1 and M1 × E1 amplitudes to the RENP process. Second, the effect of nuclear motion (vibrational states) on the molecular factor is investigated considering a single intermediate electronic state, in which we will examine how the molecular factor depends on $(A(v), X(v'))$ or $(A'(v), X(v'))$, a pair of the vibrational states on the $|e\rangle$ and $|g\rangle$ states, which may be useful in designing future experiments. Finally, the magnitudes of the molecular factor are compared for isovalent molecules, I_2, Br_2, and Cl_2, to study the dependence of the RENP rate on the spin–orbit couplings.

In order to simulate a realistic experimental situation, the I_2 energies including the spin–orbit effects are accurately calculated within the framework of the Born–Oppenheimer approximation.

Throughout this section we use atomic units. The conversion factor from the natural unit $C(\omega)$ to the atomic unit $C_{\rm au}(\omega)$ is given by

$$C(\omega) = C_0 C_{\rm au}(\omega), \quad C_0 = \epsilon_{eg}^4 \frac{e^2 a_0^2}{E_H^2} \sim 3.9 \times 10^{-12}, \tag{16}$$

with $a_0 \sim 0.53 \times 10^{-8}\,\text{cm}$, $E_H \sim 27\,\text{eV}$, $e^2 = 4\pi\alpha \sim 4\pi/137$, and using $\epsilon_{eg} = 0.810\,\text{eV}$. This gives a rate unit $\Gamma_{dm} C_0 \sim 1.0 \times 10^{-7}\,\text{Hz}$ for $n = 10^{21}\,\text{cm}^{-3}$ and $V = 10^2\,\text{cm}^3$.

3.1. Details of the calculation

The electronic excited states of the I_2 molecule were calculated by the multiconfigurational second-order perturbation method (CASPT2) [16,17], based on the reference wavefunctions obtained by the state-averaged complete active space self-consistent field (CASSCF) method [18,19] with the atomic natural orbital-relativistic correlation consistent (ANO-RCC) all-electron basis set [20]. The CASSCF method, using a linear combination of configuration state functions to describe the electronic wavefunction, is adequate for the calculation of electronically excited states with relatively small computational cost. More accurate energies, including dynamic electronic correlation, can be obtained by the CASPT2 method using the second-order perturbation to the zeroth-order CASSCF wavefunctions. The scalar relativistic effects were introduced at the CASSCF level by keeping the spin-independent (scalar) terms of the two-component reduced Hamiltonian using the fourth-order Douglas–Kroll–Hess method [21–23]. At this point, the spin–orbit effects are not included in the CASSCF wavefunctions and the CASPT2 energies. The spin–orbit effects were considered by the state-interaction method, where the spin–orbit matrix elements were evaluated between the CASSCF states using the Breit–Pauli operator [24], while the unperturbed diagonal energies were replaced by the CASPT2 energies. Final energies are obtained by diagonalization of this spin–orbit Hamiltonian. Our procedure is very similar to that employed in the calculation of the I_2 potential energy curves by Malmquist et al. [25]. D_{2h} symmetry was employed in our calculations. In the CASSCF calculation, total of 28 orbitals, 1–7a_g (i.e. $1a_g, 2a_g, \ldots, 7a_g$), 1–3b_{3u}, 1–3b_{2u}, 1b_{1g}, 1–7b_{1u}, 1–3b_{2g}, 1–3b_{3g}, and 1a_u, were kept doubly occupied. In addition, the 1a_g (1σ_g) and 1b_{1u} (1σ_u) orbitals were frozen during the calculation. The remaining 50 electrons were distributed over 26 active orbitals: 8–13a_g, 4–6b_{3u}, 4–6b_{2u}, 2b_{1g}, 8–13b_{1u}, 4–6b_{2g}, 4–6b_{3g}, and 2a_u. The state-averaging was performed over 18 electronic states: the three lowest A_g, one B_{3u}, one B_{2u}, one B_{1g}, one B_{2g}, one B_{3g}, and one A_u state with singlet spin multiplicity, and one B_{3u}, one B_{2u}, one B_{1g}, three B_{1u}, one B_{2g}, one B_{3g}, and one A_u state with triplet spin multiplicity. Note that these electronic states correlate with two iodine

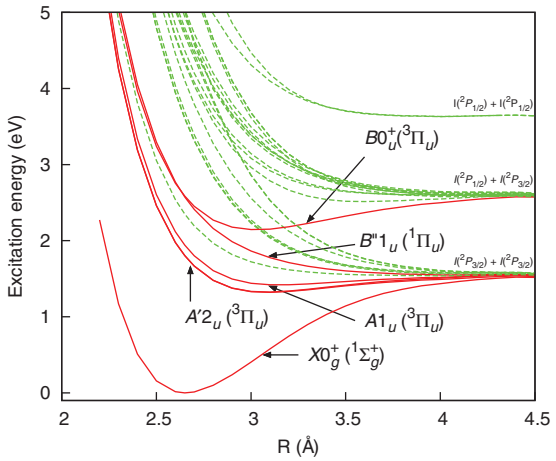

Fig. 2. Potential energy curves of the I_2 electronic states. The electronic states relevant to this work are indicated by solid red lines.

Table 1. Calculated vertical and adiabatic (T_e) excitation energies, dissociation energies (D_e), and vibrational energies (ω_e) for the I_2 X, A', A, B'', and B states. Experimental values are indicated in parentheses. [a]Reference [27]. [b]Reference [28]. [c]Reference [29]. [d]Reference [30]. [e]Unbound in the calculated result. [f]Reference [31]. [g]Reference [32]. [h]Reference [33].

State	Vertical excitation energies (eV)	T_e (eV)	D_e (eV)	ω_e (cm^{-1})
$X0_g^+(^1\Sigma_g^+)$	0.0	0.0	1.53 (1.55)[a]	220.1 (214.5)[a]
$A'2_u(^3\Pi_u)$	1.88 (1.69)[b]	1.32 (1.245)[c]	0.21 (0.311)[c]	95.3 (108.8)[c]
$A1_u(^3\Pi_u)$	1.94 (1.84)[b]	1.42 (1.353)[d]	0.11 (0.203)[d]	77.5 (88.3)[d]
$B''1_u(^1\Pi_u)$	2.57 (2.49)[b]	−[e] (1.534)[f]	−[e] (0.022)[f]	−[e] (19.8)[f]
$B0_u^+(^3\Pi_u)$	2.59 (2.37)[g]	2.14 (1.955)[h]	0.44 (0.543)[h]	117.2 (125.7)[h]

atoms in the ^2P state at the dissociation limit. By diagonalization of the spin–orbit Hamiltonian, a total of 36 spin–orbit eigenstates were obtained. All these calculations were performed using the MOLPRO suite of programs [26]. Although the electric transition dipole moments between the spin–orbit eigenstates were obtained as part of the spin–orbit calculation in the MOLPRO programs, the matrix elements of the electronic spin operator S were not provided. Thus, we explicitly evaluated the spin matrix elements between the spin–orbit eigenstates using the output of the eigenvectors.

The potential energy curves of the calculated I_2 electronic states are shown in Fig. 2. In the figure, the spin–orbit eigenstates are correlated with pairs of the atomic states $I(^2P_{3/2})+I(^2P_{3/2})$, $I(^2P_{1/2})+I(^2P_{3/2})$, or $I(^2P_{1/2})+I(^2P_{1/2})$, as the internuclear distance becomes large. The dissociation and excitation energies of the electronic states relevant to this work as well as the vibrational energies on these states are summarized in Table 1. For the purpose of this work, our results agree well with the experimental values.

3.2. Molecular factor with the fixed-nuclei approximation

In this work, we consider the I_2 $A\ 1_u(^3\Pi_u)$ and $A'\ 2_u(^3\Pi_u)$ states as the $|e\rangle$ state and the $X0_g^+(^1\Sigma_g^+)$ ground state as the $|g\rangle$ state, where the electric dipole transition between $|e\rangle$ and $|g\rangle$ is forbidden or only weakly allowed. In order to inspect which I_2 electronic states contribute to the RENP rate as the intermediate $|p\rangle$ state, we calculated $C_{\rm au}(\omega)$ at a fixed internuclear distance of 2.9 Å, which is

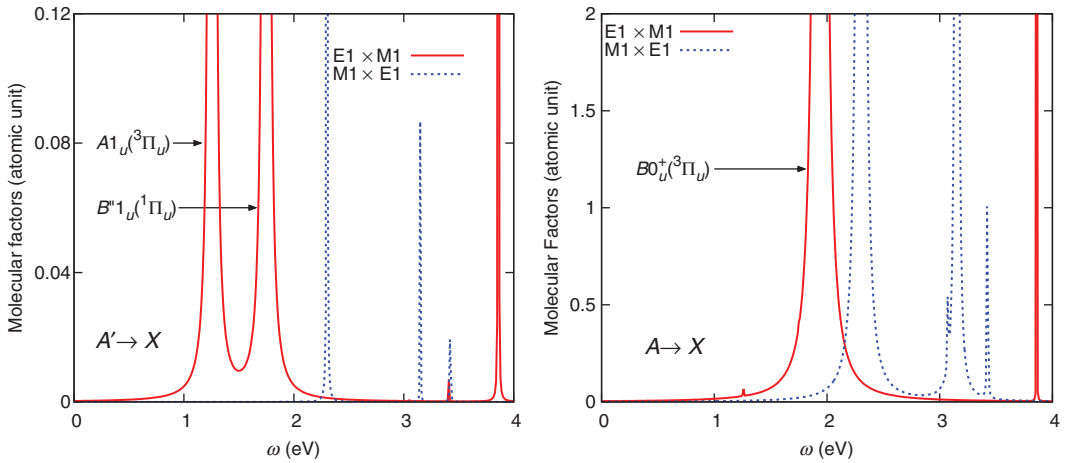

Fig. 3. Molecular factors evaluated at $R = 2.9$ Å. Left: the A' state was used as the $|e\rangle$ state. Right: the A state was used as the $|e\rangle$ state. The red line (E1 × M1, corresponding to Fig. 1(a)) represents molecular factor $C^a_{\rm au} = C^a/C_0$ in Eq. (8). The blue dashed line (M1 × E1, corresponding to Fig. 1(b)) represents molecular factor $C^b_{\rm au} = C^b/C_0$ in Eq. (17).

located between the equilibrium points of the X and A/A' states, without considering rovibrational energies. All calculated spin–orbit eigenstates are included as intermediate $|p\rangle$ states in evaluating the molecular factor $C_{\rm au}(\omega)$. In Fig. 3, the calculated molecular factor $C^a_{\rm au}(\omega)$ corresponding to Fig. 1(a) is shown along with a similar molecular factor $C^b_{\rm au}(\omega)$ corresponding to Fig. 1(b), which has an expression similar to Eq. (8) but with the spin and dipole operators being swapped as follows:

$$C^b(\omega) = \epsilon_{eg}^4 \sum_q \frac{\langle g|\vec{S}|q\rangle \cdot \langle q|\vec{S}|g\rangle \langle e|\vec{d}|q\rangle \cdot \langle q|\vec{d}|e\rangle}{(\epsilon_{qg} - \omega)^2}. \tag{17}$$

We only need energies around 0–0.5 eV in evaluating the RENP rate, although the molecular factors are plotted up to 5 eV in Fig. 3 in order to inspect the relative contribution of different intermediate electronic states. In the low-energy region below 0.5 eV, the molecular factor for the E1 × M1 process is larger than that for the M1 × E1 process in both the $A' \to X$ and $A \to X$ cases. In other words, the first term in the brackets of Eq. (4) dominates over the second term, which suggests that only the first term should be retained for the RENP using the I_2 molecule. In the plots, we can observe several spike-like structures that represent contributions of the intermediate electronic states as labeled in the figure. When the $A\ 1_u(^3\Pi_u)$ state is used as the $|e\rangle$ state, the $B\ 0^+_u(^3\Pi_u)$ state predominates among contributions from the other states. On the other hand, when the $A'\ 2_u(^3\Pi_u)$ state is used as the $|e\rangle$ state, the $A\ 1_u(^3\Pi_u)$ and $B''\ 1_u(^1\Pi_u)$ electronic states are especially important in the low-energy region relevant to this work, while the other states have negligible contributions.

From here on, only the molecular factor in Eq. (8), which corresponds to the E1 × M1 process of Fig. 1(a), will be evaluated. For the $A \to X$ process, we will consider only the B electronic state as the intermediate electronic state. For the $A' \to X$ process, the A electronic state will be mainly considered as the intermediate electronic state, since the contribution of the A state looks larger than the B'' state in the low-energy region. The validity of this approximation, including only the A electronic state in the $A' \to X$ process, will be inspected in the Appendix by comparing the amplitudes evaluated by the A intermediate electronic state and the B'' intermediate electronic state.

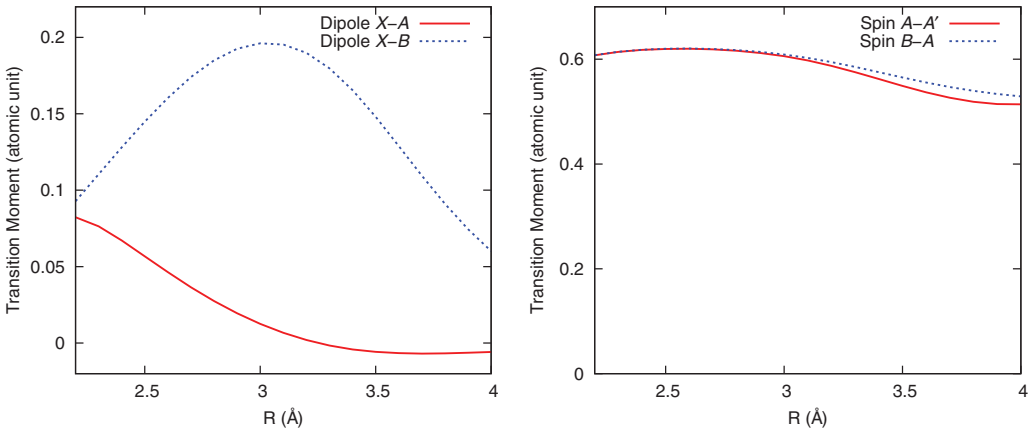

Fig. 4. Left: Electric dipole transition moment between the X and A states (red solid line), and between the X and B states (blue dashed line). Right: Spin transition moment between the A' and A states (red solid line), and between the A and B states (blue dashed line).

3.3. Molecular factor with vibrational levels on the X, A′, A, and B electronic states

Since the equilibrium internuclear distances of the X and A/A' states are rather different, proper treatment of vibrational wavefunctions may be important to estimate the RENP rate. In this section, we evaluate the molecular factors considering vibrational levels on the A', A, and X electronic states for the $A' \to X$ process, and on the A, B, and X electronic states for the $A \to X$ process. The ab initio energies of the X, A', A, and B electronic states, the same as shown in Fig. 2, were fitted using the functional form taken from Ref. [34]. The electric dipole transition moment between the X and A states and between the X and B states, and the spin transition moment between the A' and A states and between the A and B states, shown in Fig. 4, were fitted by polynomial functions. The vibrational energies and wavefunctions on each electronic state were obtained by direct diagonalization of the vibrational Hamiltonian using a pointwise coordinate representation of the wavefunctions, the discrete variable representation (DVR) method [35], with $R_{\rm min} = 2.2\,$Å, $R_{\rm max} = 7.0\,$Å, and $\Delta R = 0.006\,$Å. Summation of the intermediate vibrational states, on the A electronic state in the $A' \to X$ process, or on the B electronic state in the $A \to X$ process, was taken up to $v = 40$. These parameters for the DVR basis and the number of vibrational states in the summation were sufficient to obtain a converged result.

In Fig. 5, the calculated molecular factors at $\omega = 0.4\,$eV for the $A' \to A \to X$ process and for the $A \to B \to X$ process are shown as functions of the vibrational levels on the initial (A' or A) and final (X) electronic states. In the $A' \to A \to X$ process shown in the left-hand panel in Fig. 5, the molecular factor is largest around the point $(A'(v = 0), X(v' = 20))$. Starting from this point, the higher-intensity region extends to the upper left direction. In the $A \to B \to X$ process shown in the right-hand panel in Fig. 5, the molecular factor is largest around the point $(A(v = 0), X(v' = 24))$. In this case, the higher-intensity region extends to the upper right direction. The structure of these higher-intensity regions reflects the fact that the equilibrium points of the X and A' (or A) states are separated, and one or both of the vibrational states on these electronic states should be sufficiently excited in order to achieve favorable overlap.

In Fig. 6, the molecular factors $C^a_{\rm au}(\omega)$ for the $A' \to A \to X$ and $A \to B \to X$ processes are shown as a function of photon energy w. The vibrational level on the initial state, the A' or A electronic state, was selected to be $v = 0$, and the vibrational level on the final X electronic state was

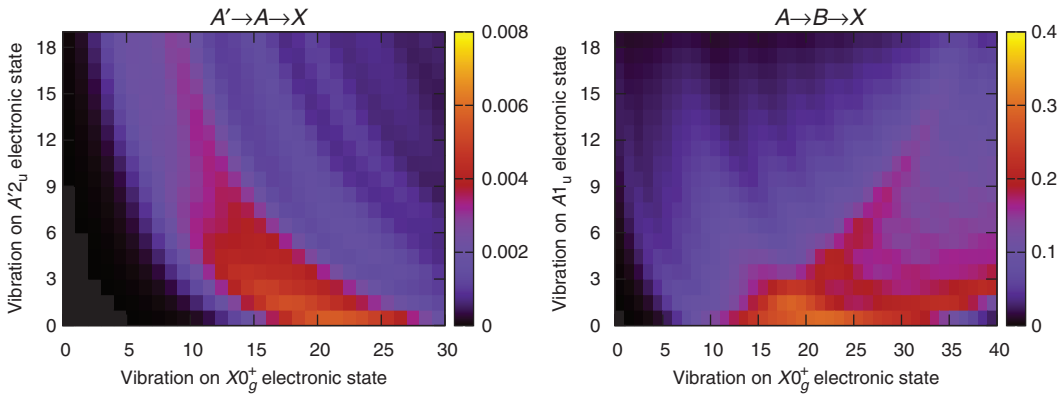

Fig. 5. Molecular factor $C^a_{\rm au}(\omega)$ at $\omega = 0.4$ eV, considering vibrational levels on the X, A', A, and B electronic states. The left-hand panel represents the process in which the initial excited electronic state is the A' state, the intermediate electronic state is the A state, and the final electronic state is the X state. The right-hand panel represents the process where the initial excited electronic state is the A state, the intermediate electronic state is the B state, and the final electronic state is the X state.

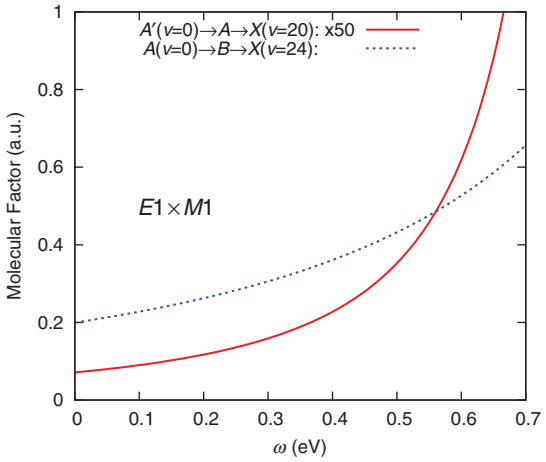

Fig. 6. Molecular factor $C^a_{\rm au}(\omega)$ as a function of photon energy ω, considering vibrational levels on the X, A', A, and B electronic states.

selected to be $v = 20$ in the $A' \to A \to X$ case, and $v = 24$ in the $A \to B \to X$ case. As shown in the figure, the molecular factor for the $A \to B \to X$ process is about 50 times larger than that for the $A' \to A \to X$ process.

3.4. Comparison with other molecules: Cl_2, Br_2, and O_2

In order to inspect the effect of atomic weight, or the strength of the spin–orbit couplings, we calculated the molecular factor $C^a_{\rm au}$ for the E1 × M1 process for the Cl_2 and Br_2 molecules with the fixed-nuclei approximation. The arrangements of the potential energy curves of Cl_2 and Br_2 are very similar to that of I_2, as shown in Fig. 7. In both Cl_2 and Br_2, the ground, first, and second lowest excited states correspond to the $X0^+_g(^1\Sigma^+_g)$, $A'2_u(^3\Pi_u)$, and $A1_u(^3\Pi_u)$ states, respectively, as in the I_2 case. Also, the location of the $B\ 0^+_u(^3\Pi_u)$ state is similar to that of the B state in the I_2 molecule. The procedure of the calculation is the same as in the I_2 case described in Sects. 3.1 and 3.2. The molecular factors were evaluated for two different pathways as in the I_2 molecule. In the first case, we took the $A'2_u(^3\Pi_u)$ state as the initial state and $X0^+_g(^1\Sigma^+_g)$ as the final state. In the second case,

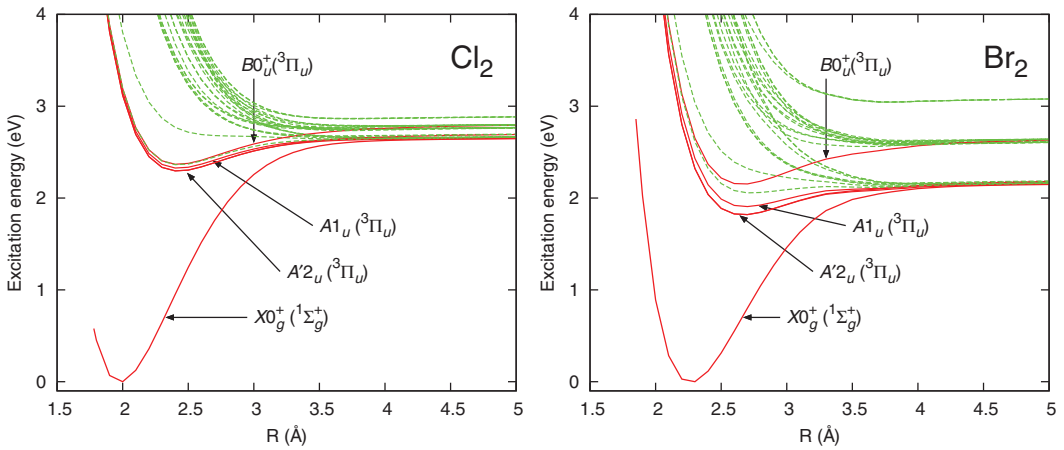

Fig. 7. Potential energy curves of Cl_2 (left) and Br_2 (right).

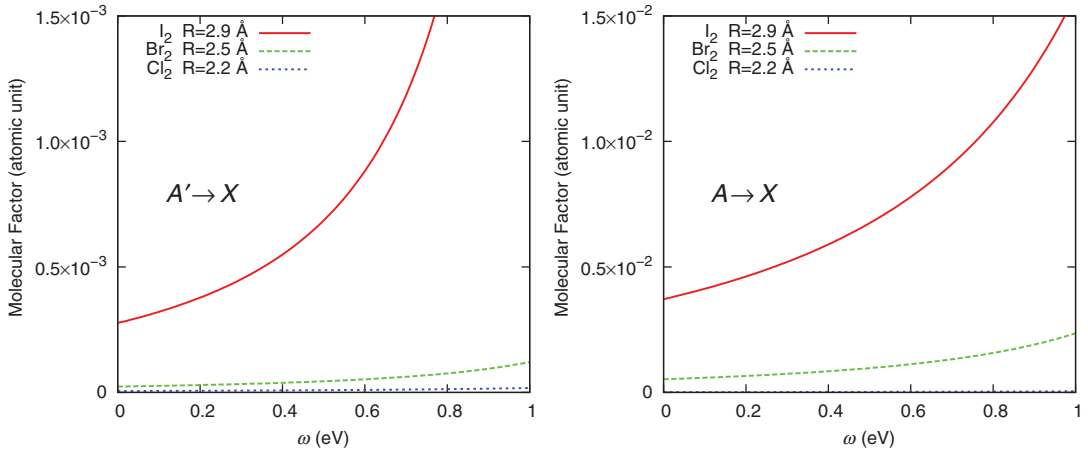

Fig. 8. Comparison of the molecular factors $C^a_{\rm au}$ in Eq. (8) for the I_2, Br_2, and Cl_2 molecules in the fixed-nuclei approximation. Left: the A' state was used as the $|e\rangle$ state. Right: the A state was used as the $|e\rangle$ state. The details of the calculation are the same as in Fig. 3.

the $A1_u(^3\Pi_u)$ state was taken as the initial state and $X0^+_g(^1\Sigma^+_g)$ was taken as the final state. The other 34 electronic states were considered in the summation of the intermediate state. We selected $R = 2.2$ and 2.5 Å for Cl_2 and Br_2, respectively, which are the middle points between the equilibrium points of the initial and final states. In Fig. 8, the molecular factors for I_2, Br_2, and Cl_2 are compared. The molecular factors for the $A \to X$ process are about 10 times larger than those for the $A' \to X$ process in all cases of I_2, Br_2, and Cl_2 molecules. The magnitude of the molecular factor is largest for I_2 and smallest for Cl_2 in both the $A' \to X$ and $A \to X$ processes. These differences in magnitudes reflect the differences in strength of the spin–orbit couplings in these three molecules.

We also investigated the lighter molecule, O_2. In this case, the metastable $c^1\Sigma^-_u$ state was selected as the initial $|e\rangle$ state, and the $X^3\Sigma^-_g$ state as the final $|g\rangle$ state. Using the same procedure as we used for I_2, Br_2, and Cl_2, the molecular factors for the E1 × M1 and M1 × E1 processes are calculated with the fixed-nuclei approximation. The molecular factor of O_2 for the E1 × M1 process is approximately 10^{-11}–10^{-10} in the energy range $\omega = 1$–2 eV, where the $A^3\Sigma^+_u$ state has the dominant contribution to the virtual state summation. For the M1 × E1 process, the molecular factor is about 10^{-7} in the energy range $\omega = 1$–2 eV, where the $1^1\Pi_g$ state has the dominant contribution to the virtual state

summation. As expected from its small spin–orbit couplings, the molecular factor for the O_2 molecule is smaller than the other I_2, Br_2, and Cl_2 molecules: the magnitudes of the molecular factors in the $A \to X$ process are $\sim 10^{-2}$, $\sim 10^{-3}$, and $\sim 10^{-4}$, respectively.

4. RENP spectral rate

The large macroscopic polarization necessary for significant RENP rates is developed by two trigger laser irradiations of frequencies ω and ω' with $\omega + \omega' = \epsilon_{eg}$. The RENP amplitude is proportional to the polarization $\langle g|(R_1 - iR_2)/2|p\rangle$ averaged over intermediate states $|p\rangle$. Hence the transition to a final single vibrational state $X(v')$ for $|g\rangle$ is selected out for the macro-coherently amplified RENP at each experimental setup.

Before the detailed presentation of numerical results, it is appropriate to explain how neutrino properties and parameters may be determined experimentally. Suppose that two continuous-wave trigger lasers of frequencies $\omega + \omega' = \epsilon_{eg}$ are irradiated in counter-propagating directions and two exciting pulse lasers of frequencies $\omega_P - \omega_S = \epsilon_{eg}$ (in order to induce a Raman-type excitation $|g\rangle \to |e\rangle$) are suddenly switched on. Only during this pulse irradiation does RENP occur, giving a unique signal: asymmetric directional increase of the light output of lower frequency ω. If statistics allows, one may hope to measure parity-violating quantities such as the emergence of circular polarization from linear polarization. Parity-violating quantities that indicate unambiguous signals of involved weak interaction appear with rates at least 100 times smaller than parity-conserving quantities do. Observations at different combinations of (ω, ω') provide spectrum rates at different ω values, thus covering some range of frequencies that gives the experimentally observed spectrum. After this spectrum determination, one compares the data with the theoretical prediction computed assuming some values of undetermined neutrino parameters and properties, and finally the best fit with theoretical calculation determines these parameters.

The experimental method sketched here is by no means unique, and one can think of other schemes. Moreover, many simulations have to be done to determine the signal level once the best method of background rejection is found. It is suggested that the most serious background of the two-photon process may be rejected by the formation of condensed solitons [5], which are a target state of a coherent macroscopic target entangled by static field condensates.

The quantity $C^a(\omega)I(\omega)/C_0 = C^a_{\rm au}(\omega)I(\omega)$ in atomic units is plotted in the following figures, except in the last three figures where absolute rates are illustrated for the target parameters of $n = 10^{21}\,{\rm cm}^{-3}$ and $V = 10^2\,{\rm cm}^3$. For calculation of the spectral rate, we used numerical values of the mixing angles θ_{12}, θ_{13}, as determined in neutrino oscillation experiments, Eq. (2), thus giving numerical weights for the six thresholds in Table 2. (As usual, the conventional definition of oscillation angle factors $c_{ij} = \cos\theta_{ij}, s_{ij} = \sin\theta_{ij}$ is used in this table.) We also used mass constraints given by oscillation data, Eq. (2). The smallest mass defined by m_0 differs in the NH case where $m_0 = m_1 (< m_2 < m_3)$ and in the IH case where $m_0 = m_3 (< m_1 < m_2)$. For large m_0, the NH and IH differences are relatively small: for instance, in the NH case $m_0 = 100\,{\rm meV}$ gives three neutrino masses, $m_1 = 100$, $m_2 = 100.37$, and $m_3 = 111.8\,{\rm meV}$, while in the IH case $m_0 = 100\,{\rm meV}$ gives $m_3 = 100$, $m_1 = 111.8$, and $m_2 = 112.1\,{\rm meV}$, their mass range within $\sim 10\%$. The mass pattern for a large m_0 has been called the quasi-degenerate case.

In all spectral rate figures we take as the initial state the I_2 $A(v = 0)$ state and as the final state various vibrational states of $X(v')$. It turns out that the numerically dominant contributions are to $X(v' = 22$–$26)$. Below, we consider $X(v' = 24)$ as a representative example, since the molecular factors for $X(v' = 22$–$26)$ are almost identical. For simplicity we have omitted contributions from

Table 2. The threshold weight $B_{ij} = |a_{ij}|^2 = |U_{ei}^* U_{ej} - \delta_{ij}/2|^2$.

B_{11}	B_{22}	B_{33}	$B_{12} + B_{21}$	$B_{23} + B_{32}$	$B_{31} + B_{13}$
$(c_{12}^2 c_{13}^2 - 1/2)^2$	$(s_{12}^2 c_{13}^2 - 1/2)^2$	$(s_{13}^2 - 1/2)^2$	$2c_{12}^2 s_{12}^2 c_{13}^4$	$2s_{12}^2 c_{13}^2 s_{13}^2$	$2c_{12}^2 c_{13}^2 s_{13}^2$
0.030	0.039	0.23	0.41	0.015	0.032

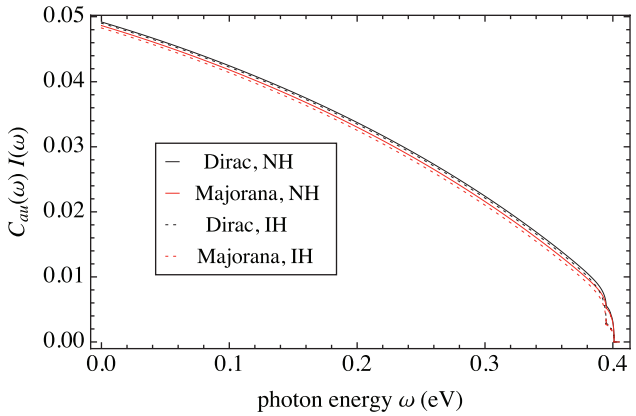

Fig. 9. I_2 spectrum $C_{\rm au}(\omega) I(\omega)$ taking $\bar{\epsilon} = \epsilon_{eg} = 0.810\,\text{eV}$ for the transition $A(v = 0) \to X(v' = 24)$. The Dirac NH case in solid black, Majorana NH case of $(\alpha, \beta') = (0, 0)$ in solid red are compared with the IH cases in dashed colors, taking the smallest neutrino mass of 40 meV.

intermediate states other than the B state, but included all numerically significant vibrational states of $B(v'')$ as the intermediate state $|p\rangle$. The RENP spectral rate from the metastable A' state is calculated in a similar way. The dominant contribution arises from $X(v' = 20)$. However, the absolute rate is $\sim$50 times smaller than in the case of $A(v = 0) \to X(v' = 24)$.

In Fig. 9 a global photon spectrum in the entire energy region is shown for the transition $A(v = 0) \to X(v' = 24)$, where four different cases are plotted: NH Dirac in a black solid line, NH Majorana of $(\alpha, \beta - \delta) = (0, 0)$ (the CP-conserving case) in red solid, IH Dirac in black dashed, and IH Majorana in red dashed (all with the smallest neutrino mass of 40 meV)[4]. All these cases appear nearly degenerate in the plot.

On the other hand, the enlarged spectrum in the threshold region is shown for smaller mass values of m_0 in Fig. 10. One can clearly observe three kinks in the NH case, which are identified as photon energy thresholds of (11), (12), and (22). The other three threshold kinks, (13), (23), and (33), in the NH case are further to the left in this figure. This figure suggests a good chance of determining the smallest neutrino mass at the precision level of 1 meV, if one has plenty of statistical data in the threshold region.

We shall next examine the possibility of Majorana–Dirac distinction along with determination of CPV phases. The relevant CPV phases α, β, δ in the Majorana case appear in the matrix elements as

$$U_{e1} = \cos\theta_{13}\cos\theta_{12}, \quad U_{e2} = \cos\theta_{13}\sin\theta_{12} e^{i\alpha}, \quad U_{e3} = \sin\theta_{13} e^{i(\beta-\delta)}. \tag{18}$$

In the Dirac case there is no CPV phase dependence of the photon energy spectrum rate to this approximation. The parameter δ alone is accessible independently in neutrino oscillation experiments. These

[4] Due to a non-trivial ω dependence of the molecular factor $C^a(\omega)$ as calculated in the preceding section, the overall spectral form shown in Fig. 9 is considerably different from the one previously given in Ref. [5], where the precise calculation of $C^a(\omega)$ is not attempted and the ω dependence of $C^a(\omega)$ has been ignored.

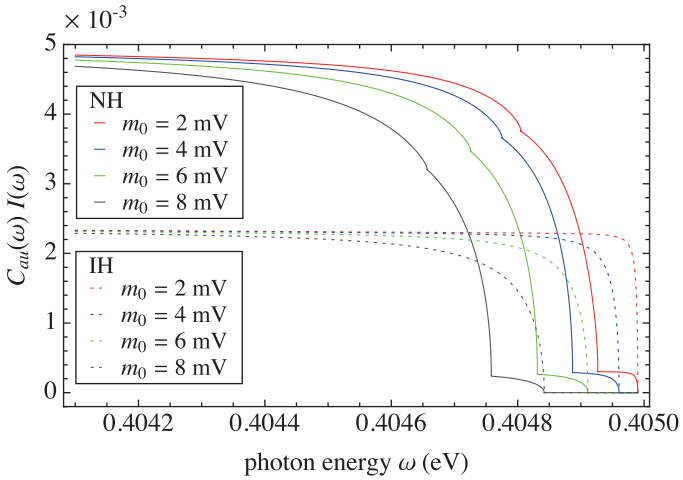

Fig. 10. Sensitivity of spectral shape to the smallest neutrino mass values 2, 4, 6, 8 meV compared for the Majorana case of $(\alpha, \beta') = (0, 0)$: NH (solid) and IH (dashed) cases.

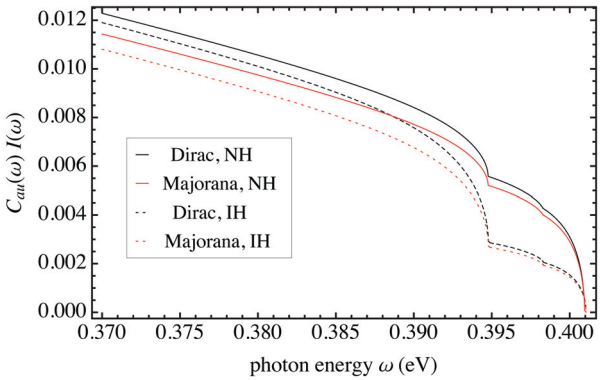

Fig. 11. CP-conserving Majorana case of $(\alpha, \beta') = (0, 0)$ vs Dirac distinction; Dirac in black, Majorana in red. The smallest neutrino mass of 40 meV, NH (solid), and IH (dashed) cases are assumed.

phases appear multiplicatively, in the rate formula around three thresholds of (12), (13), and (23), as

$$\cos 2\alpha, \quad \cos 2(\beta - \delta), \quad \cos 2(\alpha - \beta + \delta), \tag{19}$$

which are further multiplied by the weight factor of Table 2 [5] times the product of two masses $m_i m_j$, $i \neq j$. There is thus no doubt that the Majorana–Dirac distinction is easier for larger neutrino masses. We shall introduce a new notation for the CPV phase $\beta' \equiv \beta - \delta$ to simplify the formulas. The case $(\alpha, \beta') = (0, 0)$ corresponds to CP-conserving (CPC) Majorana neutrino pair emission.

As is evident in Fig. 11, the Majorana–Dirac distinction in the proposed de-excitation of I_2 appears easier than the NH–IH distinction at low enough photon energies where rates are largest. Numerically, the I_2 CPC Majorana rate for $m_0 = 40$ meV is significantly different from the Dirac rate by ~ 0.07 at a photon energy 0.37 eV, while this difference for the Xe $J = 2$ transition [5] never exceeds 0.2% at all photon energies.

Study of the sensitivity to the CPV phase α, β', however, requires a more careful analysis, because the CPC case of $(\alpha, \beta') = (0, 0)$ gives the largest destructive interference due to the effect of identical Majorana fermions; hence, the Majorana–Dirac distinction is easiest in this case. It is thus necessary to vary the CPV phases (α, β') in their allowed range. It turns out that, with the given numerical weight factors of Table 2, the dependence of spectral rates on β' is much weaker than on α. The most

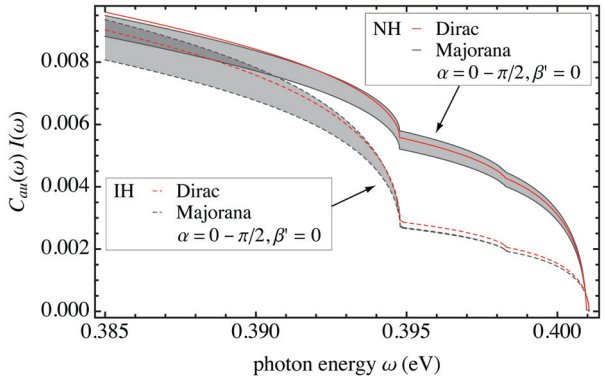

Fig. 12. Majorana α-band and Dirac photon spectrum for $A(v = 0) \to X(v' = 24)$. The Majorana band is defined by variation of α in the range 0–$\pi/2$ with a fixed $\beta' = 0$. Dirac NH is given in solid red and Dirac IH in dashed red, while the upper (lower) band corresponds to NH (IH). The smallest neutrino mass of 40 meV is assumed.

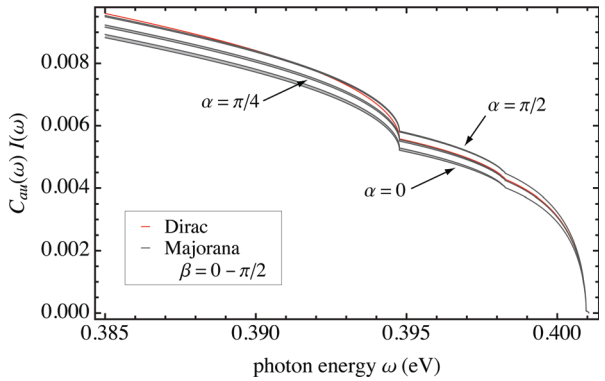

Fig. 13. Majorana β-bands (shaded region bounded by black curves) for 3 values of $\alpha = 0, \pi/4, \pi/2$ that are well separated, and the Dirac (red) photon spectrum for $A(v = 0) \to X(v' = 24)$. A Majorana β-band is defined by the variation of β in the range 0–$\pi/2$ with a fixed α. The NH case is shown. The smallest neutrino mass of 40 meV is assumed.

prominent kinks are at the (12) and (33) thresholds and the highest sensitivity to α arises from the (12) threshold. Under these circumstances we may introduce the useful concept of the Majorana α-band, which is defined by the region of spectral rates, bounded by the largest Majorana rate at $\alpha = \pi/2$ and the smallest rate at $\alpha = 0$. We illustrate this band structure in Fig. 12. Strictly, the α-band is defined for $\beta' = 0$, but the dependence of the band shape on β' is small and we may approximately use the α-band terminology for any value of β'.

On the other hand, variation of β' gives much smaller band widths, and moreover these bands are separated as α values vary, as shown in Fig. 13. This implies that experimental determination of β' is much more difficult than α in the proposed I_2 de-excitation scheme. We shall concentrate on determination of the CPV parameter α in the following.

The spectral rate for a large value of the smallest neutrino mass, 250 meV (a quasi-degenerate mass not excluded by the cosmological bound [4]), is shown in Fig. 14, which shows a great sensitivity to the Majorana–Dirac distinction for this quasi-degenerate case. Another example of spectral rate is shown for $m_0 = 100$ meV in Fig. 15, where the Dirac case and the Majorana case of $\alpha = \pi/2$ become nearly degenerate in the plot. Thus, for relatively smaller mass values of m_0 one needs more detailed

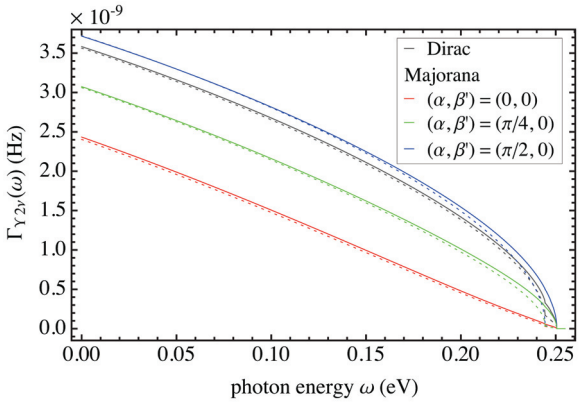

Fig. 14. Three Majorana cases and the Dirac case of the photon spectrum for $A(v=0) \to X(v'=24)$; NH in solid and IH in dashed. Different colors correspond to the Dirac and a few Majorana cases; Dirac in black, Majorana of $(\alpha, \beta) = (0, 0)$ in red, Majorana of $(\alpha, \beta) = (\pi/2, 0)$ in blue, and Majorana of $(\alpha, \beta) = (\pi/4, 0)$ in green. The smallest neutrino mass of 250 meV is assumed. The transition $A(v=0) \to X(v'=25)$ gives similar but slightly smaller rate curves.

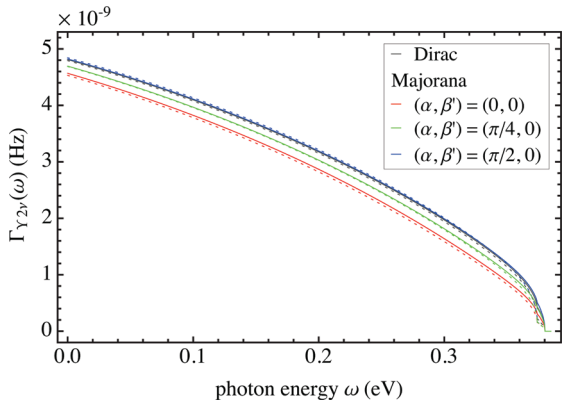

Fig. 15. Similar plot to Fig. 14 for $m_0 = 100$ meV and $A(v=0) \to X(v'=24)$.

study, both by theoretical means and numerical simulations, for determination of the α parameter, which is beyond the scope of the present work.

It is important to note that comparison of two de-excitations to $X(v'=24$ and $25)$ offers a good tool for unambiguous experimental identification of RENP (this can be done by a change of one of the two trigger lasers). This is an advantage of molecular targets, since one may compare two spectra of different transitions without relying too heavily on the absolute rate scale. The zero photon energy limit of the absolute spectrum gives an overall magnitude of the RENP rate, which then indicates the relative difference between these two different transitions. We plot in Fig. 16 these values for transitions to $X(v'=24$ and $25)$ as functions of the smallest neutrino mass m_0, which shows insensitivity of rates for $m_0 < O(30)$ meV. There is an interesting phenomenon of crossover of rates occurring at two points of the smallest mass $m_0 \sim 140$ meV and $\sim$390 meV. For the range of the α parameter between these two values, the Dirac and Majorana $(\pi/2, 0)$ rates to $X(v'=25)$ of smaller atomic energy separation overtake the Majorana $(0, 0)$ rate to $X(v'=24)$ of larger separation. The simultaneous use of different vibrational transitions of molecules may be effective for RENP identification and exploration of the neutrino mass range as well.

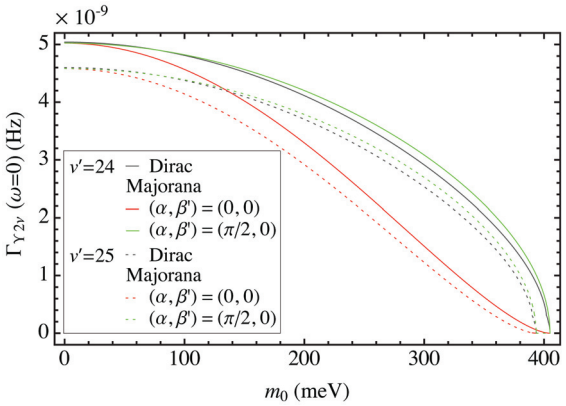

Fig. 16. Zero energy limits of NH absolute spectrum rates (in units of 10^{-11} Hz) are shown for two transitions to $X(v' = 24)$ (solid) and $X(v' = 25)$ (dashed). The Dirac cases are given in black, while the Majorana cases of $(\alpha, \beta) = (0, 0)$ are given in red and the $(\pi/2, 0)$ cases are in green. The target parameters are $n = 10^{21}$ cm^{-3} and $V = 10^2$ cm^3. $\epsilon_{eg} = 0.787$ eV was used for $X(v' = 25)$.

The actual rate at each photon energy is equal to the plotted values $C_{\rm au}(\omega)I(\omega)$ multiplied by the factor

$$\Gamma_{dm}C_0 \sim 1.0 \times 10^{-7}\,{\rm Hz}\left(\frac{n}{10^{21}\,{\rm cm}^{-3}}\right)^3 \frac{V}{10^2\,{\rm cm}^3}\left(\frac{\epsilon_{eg}}{0.810\,{\rm eV}}\right)^3. \tag{20}$$

Note that we took $\eta_\omega(t) = 1$, which is, however, expected to be smaller than 1.

Let us compare the I_2 RENP rate with the Xe rate. The I_2 rate is calculated as $\sim$5 nHz at $\omega = 0$, assuming targets with $n = 10^{21}$ cm^{-3}, $V = 10^2$ cm^3, and $\eta_\omega = 1$. Under the same experimental conditions for the targets, the overall RENP rate for the Xe atom is much larger, by $\sim 10^5$. The origin of this large rate difference is explained as follows. The dependence of the RENP rate (for definiteness at $\omega = 0$) is roughly given by the product of factors as

$$\Gamma_{\gamma 2\nu}(0) \propto G_F^2 n^3 V d^2 S^2 \frac{\epsilon_{eg}^3}{\epsilon_{pg}^2}, \tag{21}$$

where we used d and S to mean the magnitudes of the dipole and the spin factor in the RENP amplitude. The relation $\epsilon_{eg} \approx \epsilon_{pg}$ approximately holds for both Xe and I_2. An extra n-dependence in addition to the basic macro-coherence dependence $\propto n^2$ arises by our assumption of taking the maximal RENP rate ($\eta_\omega = 1$), with the stored field energy density of $|\vec{E}|^2 = \epsilon_{eg} n$. The difference of ϵ_{eg} between Xe and I_2 is $\sim$10 and the spin factor is of the same order of unity for the two targets. The Franck–Condon-like suppression factor[5] intrinsic to molecules is only 0.03 for I_2. The rest of the rate difference by $\sim$300 is attributed to the difference in the transition dipole moments of Xe and I_2. Unlike the simple dipole transition $6s \to 5p$ in the Xe atom, the I_2 molecular dipole arises from $B(^3\Pi_u) \to X(^1\Sigma_g^+)$ involving different configurations and is greatly suppressed. We definitely need a solid environment of the target number density of $O(10^{23})$ cm^{-3} for realistic I_2 RENP experiments, which is a challenge left to experimentalists. A molecule closer to Xe with respect to RENP appears to be CsI.

[5] In Ref. [5] the Franck–Condon factor of I_2 was calculated using the Morse potential, where relevant parameters are determined by experimental data. Our new rate estimate for the transition $A(v = 0) \to X(v' = 24)$ gives a value $\sim$ 0.03 arising from the Franck–Condon factor.

5. Summary

An attractive feature of using molecules is that there are many vibrational states available as a final molecular state for RENP, which makes experimental identification of the process easier. We computed the RENP spectrum rate for homonuclear diatomic molecules of the isovalent series Cl_2, Br_2, and I_2 and found that the rate becomes larger as the atomic number increases, as is expected. Even the largest I_2 rate is, however, much smaller than the Xe atom rate. The distinction of Majorana–Dirac neutrinos and the determination of some range of the new CPV phase α are possible at photon energies where rates are largest for the quasi-degenerate neutrino masses. The NH–IH distinction along with the smallest mass measurement can be done around the threshold region.

Acknowledgment

This research was partially supported by a Grant-in-Aid for Scientific Research on Innovative Areas Extreme Quantum World Opened up by Atoms (Grant Nos. 21104002 and 21104003) from the Ministry of Education, Culture, Sports, Science, and Technology of Japan. M.T. and M.E. thank JSPS for financial support.

Appendix A. Comparison of the contributions from the A and B'' states in the I_2 $A' \to X$ process, including the effect of nuclear motion

In the left-hand panel of Fig. 3, with the fixed-nuclei approximation, the contribution of the B'' state to the molecular factor in the $A' \to X$ process looks close to that of the A state in the low-energy region. Although we calculated the molecular factor for the $A' \to X$ process considering only the A intermediate state in Sect. 3.3, it is not clear if the A state has a significantly larger contribution to the molecular factor $C^a_{\rm au}$ for the E1 $\times$ M1 process than the B'' state, when the effect of nuclear motion is considered. Here, we evaluate the amplitude of the first term in the brackets of Eq. (4), including nuclear motion, separately for the A and B'' states, and estimate their contributions to the molecular factor. The reason for not treating the molecular factor $C^a_{\rm au}$ directly but evaluating the first term in the brackets of Eq. (4) is that the B'' state is repulsive—see Fig. 2—and it is difficult to treat continuum nuclear wavefunctions in the expression of Eq. (8). The first term in the brackets of Eq. (4), on the other hand, can be easily evaluated using the following expression:

$$\sum_p \frac{\langle g|d|p\rangle\langle p|S|e\rangle}{E_p - E_g - \omega} = \lim_{\epsilon\to+0} i\int_0^\infty dt e^{it(\omega+E_g)}\langle g|de^{-it(\hat{H}-i\epsilon)}S|e\rangle \tag{A1}$$

where $\hat{H}|p\rangle = E_p|p\rangle$ is assumed. This equation represents the Green's function by integral in the time domain [36], and can be evaluated by the Fourier transform of the correlation function $\langle g|de^{-it(\hat{H}-i\epsilon)}S|e\rangle$ obtained by solving the time-dependent Schrödinger equation. For our purpose, the vibrational (nuclear) Hamiltonian on the A or B'' electronic state is used for $\hat{H}$.

As a test, we evaluated the right- and left-hand sides of Eq. (A1) separately for the I_2 $A' \to A \to X$ process using explicit summation of the vibrational states, and the wavepacket propagation on the A state, respectively. The same DVR basis parameters were used as in Sect. 3.3. The wavepacket was propagated by expanding the time evolution operator in terms of Chebyshev polynomials [37], with $\Delta t = 0.1$ fs. Since many bound vibrational eigenstates contribute to the time evolution of the wavepacket, we need a relatively long total propagation time, 7.0 ps. In addition, we had to leave a small but finite value of ϵ, 10^{-4} au, in order to converge the Fourier transform in the right-hand side of Eq. (A1). As shown in Fig. A1, numerical values of the left- and right-hand sides of Eq. (A1) agree perfectly well in the A electronic state case.

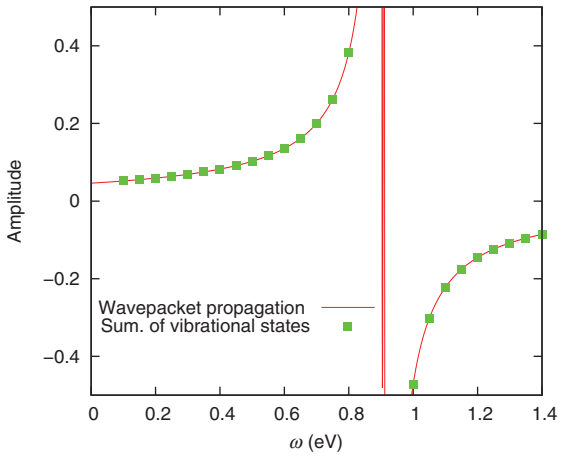

Fig. A1. Comparison of Eq. (A1) evaluated by the vibrational state summation ($v = 0$–19) and the wavepacket propagation on the I_2 $A1_u$ intermediate electronic state, using the I_2 $A'(v = 0)$ state as the initial state, and the $X(v' = 20)$ state as the final state.

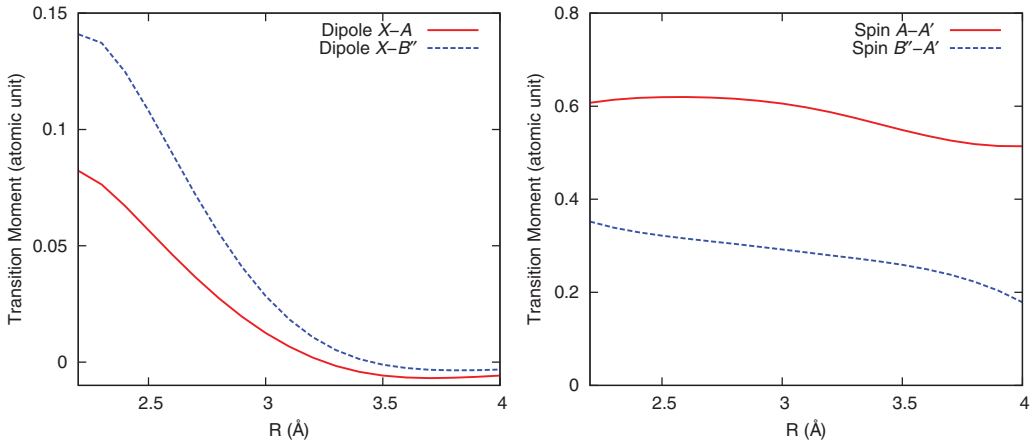

Fig. A2. Left: Electric dipole transition moment between the X and A states of I_2 (red solid line), and between the X and B'' states (blue dashed line). Right: Spin transition moment between the A and A' states (red solid line), and between the B'' and A' states (blue dashed line).

For the wavepacket calculation on the B'' state, the same DVR basis parameters were used. Since the B'' state is repulsive, we need to put the absorbing potential from $R = 5.0$ to 7.0 Å to prevent artificial reflection of the wavepacket at the boundary. This absorbing potential can be regarded as decay of the wavepacket into $R = \infty$. The wavepacket on the B'' potential energy curve with the specific initial state $S|A'(v)\rangle$, where $A'(v)$ represents the vibrational state on the A' state, is propagated by expanding the time evolution operator in terms of Chebyshev polynomials [37], with $\Delta t = 0.1$ fs. The total propagation time is 400 fs, which is much shorter than the time needed in the wavepacket propagation on the A electronic state. This short propagation time can be attributed to the fact that the wavepacket is not reflected, but just absorbed in 400 fs at the right-hand side of the B'' potential energy curve. The dipole and spin transition moments, necessary to evaluate Eq. (A1), are shown in Fig. A2.

The amplitudes for the $A' \rightarrow X$ process with the A and B'' intermediate electronic states, obtained by the wavepacket calculations, are compared in Fig. A3. When the initial vibrational state is $A'(v = 0)$ and the final vibrational state is $X(v' = 20)$, the amplitude of the A state at $\omega = 0.4$ eV

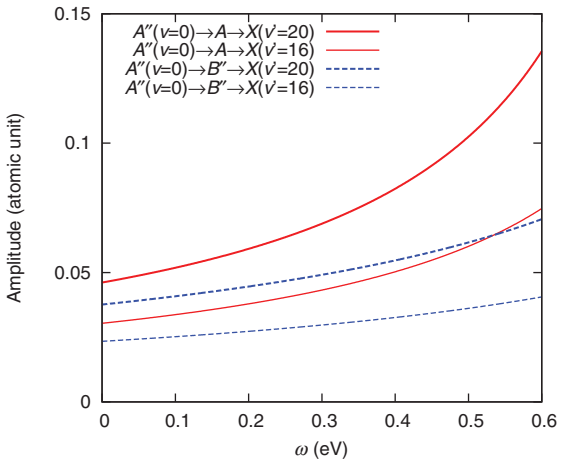

Fig. A3. Comparison of the amplitudes, Eq. (A1), with the $A1_u$ and $B''1_u$ intermediate electronic states, obtained by the wavepacket calculations. The initial states are $A'(v = 0)$, and the final states are $X(v' = 16, 20)$.

is about 60% larger than that of the B'' state. This means that the molecular factor including the A intermediate state is approximately 2.5 times larger than that including the B'' intermediate state. Although the contribution of the B'' state is not negligible, for the purpose of the present study, the molecular factor may be safely approximated by including only the A electronic state.

Funding

Open Access funding: SCOAP[3].

References

[1] G. L. Fogli, E. Lisi, A. Marrone, D. Montanino, A. Palazzo, and A. M. Rotunno, Phys. Rev. D **86**, 013012 (2012).
[2] M.C. Gonzalez-Garcia, M. Maltoni, J. Salvado, and T. Schwetz, J. High Energy Phys. **2012**, 1 (2012).
[3] D. V. Forero, M. Tórtola, and J. W. F. Valle, Phys. Rev. D **86**, 073012 (2012).
[4] J. Beringer et al., Phys. Rev. D **86**, 010001 (2012).
[5] A. Fukumi et al., Prog. Theor. Exp. Phys. **2012** [arXiv:1211.4904v1].
[6] E. D. Commins and P. H. Bucksbaum, *Weak Interactions of Leptons and Quarks* (Cambridge University Press, New York, 1983).
[7] M. Yoshimura, N. Sasao, and M. Tanaka, Phys. Rev. A **86**, 013812 (2012) [arXiv:1203.5394].
[8] M. Yoshimura, Phys. Lett. B **699**, 123 (2011) [arXiv:1203.5394].
[9] D. N. Dinh, S. Petcov, N. Sasao, M. Tanaka, and M. Yoshimura, Phys. Lett. B **719**, 154 (2012) [arXiv:1209.4808].
[10] M. Fukugita and T. Yanagida, Phys. Lett. B **174**, 45 (1986).
[11] S. Davidson and A. Ibarra, Nucl. Phys. B **648**, 345 (2003), and references therein.
[12] R. S. Mulliken, J. Chem. Phys. **55**, 288 (1971).
[13] C. Teichteil and M. Pelissier, Chem. Phys. **180**, 1 (1994).
[14] W. A. de Jong, L. Visscher, and W. C. Nieuwpoort, J. Chem. Phys. **107**, 9046 (1997).
[15] G. Herzberg, *Molecular Spectra and Molecular Structure: I. Spectra of Diatomic Molecules* (Krieger Publishing, Malabar, FL, 1989), 2nd ed.
[16] H.-J. Werner, Mol. Phys. **89**, 645 (1996).
[17] P. Celani and H.-J. Werner, J. Chem. Phys. **112**, 5546 (2000).
[18] P. J. Knowles and H.-J. Werner, Chem. Phys. Lett. **115**, 259 (1985).
[19] H.-J. Werner and P. J. Knowles, J. Chem. Phys. **82**, 5053 (1985).
[20] B. O. Roos, R Lindh, P. A. Malmqvist, V. Veryazov, and P. O. Widmark, J. Phys. Chem. A **108**, 2851 (2004).

[21] M. Reiher and A. Wolf, J. Chem. Phys. **121**, 2037 (2004).
[22] M. Reiher and A. Wolf, J. Chem. Phys. **121**, 10945 (2004).
[23] A. Wolf, M. Reiher, and B. A. Hess, J. Chem. Phys. **117**, 9215 (2002).
[24] A. Berning, M. Schweizer, H.-J. Werner, P. J. Knowles, and P. Palmieri, Mol. Phys. **98**, 1823 (2000).
[25] P. A. Malmqvist, B. O. Roos, and B Schimmelpfennig, Chem. Phys. Lett. **357**, 230 (2002).
[26] H.-J. Werner et al., Molpro, version 2010.1, a package of ab initio programs (2010).
[27] T. Ishiwata, H. Ohtoshi, M. Sakaki, and I. Tanaka, J. Chem. Phys. **80**, 1411 (1984).
[28] J. Tellinghuisen, J. Chem. Phys. **58**, 2821 (1973).
[29] J. B. Koffend, A. M. Sibai, and R. Bacis, J. Phys. (France) **43**, 1639 (1982).
[30] S. Gerstenkorn, P. Luc, and J. Verges, J. Phys. B **14**, L193 (1981).
[31] J. Tellinghuisen, J. Chem. Phys. **82**, 4012 (1985).
[32] J. Tellinghuisen, J. Chem. Phys. **76**, 4736 (1982).
[33] F. Martin, R. Bacis, S. Churassy, and J. Verges, J. Mol. Spectrosc. **116**, 71 (1986).
[34] A. J. C. Varandas, Adv. Chem. Phys. **74**, 255 (1988).
[35] D. T. Colbert and W. H. Miller, J. Chem. Phys. **96**, 1982 (1992).
[36] R. D. Levine, *Quantum Mechanics of Molecular Rate Processes* (Clarendon Press, Oxford, 1969), p. 19.
[37] H. Tal-Ezer and R. Kosloff, J. Chem. Phys. **81**, 3967 (1984).